energies

MDPI

Article

Infiltrated $Ba_{0.5}Sr_{0.5}Co_{0.8}Fe_{0.2}O_{3-\delta}$-based electrodes as anodes in solid oxide electrolysis cells

Xavier Majnoni d'Intignano [1], Davide Cademartori [2], Davide Clematis [2], Sabrina Presto [3], Massimo Viviani [3], Rodolfo Botter [2], Antonio Barbucci [2,3], Giacomo Cerisola [2], Gilles Caboche [1] and M. Paola Carpanese [2,3] *

[1] ESIREM-ICB-UMR6303, CNRS – Université de Bourgogne Franche-Comté, 9 Avenue Savary, BP47870 21078 DIJON Cedex, France; (X.M.I.) Xavier_Majnoni-D-Intignano@etu.u-bourgogne.fr; (G.Cab.) gilles.caboche@u-bourgogne.fr

[2] DICCA-UNIGE, Via all'Opera Pia 15, 16145 Genova, Italy; (D.Cad.) davidecade95@gmail.com; (D.Cle.) davide.clematis@edu.unige.it; (R.B.) rodolfo.botter@unige.it; (R.B.); (A.B.) barbucci@unige.it; (G.Cer.) giacomo.cerisola@unige.it; (M.P.C.) carpanese@unige.it

[3] CNR-ICMATE, c/o DICCA-UNIGE, Via all'Opera Pia 15, 16145 Genova, Italy; (S.P.) sabrina.presto@cnr.it; (M.V.) massimo.viviani@ge.icmate.cnr.it; (A.B.) barbucci@unige.it; (M.P.C) carpanese@unige.it

* Correspondence: carpanese@unige.it; Tel.: +39-010-335-6020

Received: date; Accepted: date; Published: date

Abstract: In the last decades, several works have been carried out on solid oxide fuel cell (SOFC) and solid oxide electrolysis cell (SOEC) technologies, as they are powerful and efficient devices for energy conversion and electrochemical storage. By increasing use of renewable sources, a discontinuous amount of electricity is indeed released and reliable storage systems represent the key feature in such a future energy scenario. In this context, systems based on reversible solid oxide cells (rSOC) are gaining increasing attention. An rSOC is an electrochemical device that can operate sequentially between discharging (SOFC mode) and charging (SOEC mode) then it is essential the electrodes to be able to guarantee high catalytic activity both in oxidation and reduction conditions. $Ba_{0.5}Sr_{0.5}Co_{0.8}Fe_{0.2}O_{3-\delta}$ (BSCF) has been widely recognised as one of the most promising electrode catalysts for the oxygen reduction reaction (ORR) in SOFC technology, because of its astonishing content of oxygen vacancies, even at room temperature. The purpose of this study is the development of BSCF to be used as anode material in electrolysis mode, maintaining enhanced energy and power density. Impregnation with $La_{0.8}Sr_{0.2}MnO_3$ (LSM) discrete nanolayer is applied to pursue a structural stability, resulting in a long life time reliability. Impedance spectroscopy measurements under anodic overpotential conditions is run to test BSCF and LSM-BSCF activity as electrode in oxidation mode. The observed results suggest that BSCF is a very promising candidate as oxygen electrode in rSOC systems.

Keywords: BSCF; SOEC; SOFC; rSOC; anodic overpotential; impedance spectroscopy.

1. Introduction

The increasing penetration of renewable energy sources in the power market, guided by new energy policies to address the climate change, poses new challenges that need to be tackled [1]. The intermittent nature of wind and solar power requires the development of large-scale energy storage as a key to improve the flexibility of the electric grid. Electrical energy storage (EES) is envisioned as the key factor to boost the development of advanced grid-energy management systems [2,3]. In this context, systems based on reversible solid oxide cells (rSOC) are gaining increasing attention and interest. An rSOC is an electrochemical device that can operate in both power producing (Solid Oxide Fuel Cells, SOFC) and energy storage (Solid Oxide Electrolysis Cells, SOEC) modes. The system operates sequentially between discharging (SOFC) and charging (SOEC) modes [4-9].

Electrochemical reactions can be based on either H-O or H-O-C elemental systems. In H-O systems only hydrogen, water and oxygen are involved while in H-O-C ones also hydrocarbons participate in reactions. SOFC converts hydrogen-rich fuels into electricity and heat [10]. On the other side, the electricity supplied to SOEC leads to the conversion of H_2O and CO_2 into a syngas usually containing H_2 and CO [11]. Water electrolysis can also be performed by either alkaline or proton exchange membrane electrolysers. The most commercial electrolysers up to date belong to the alkaline series with sizes ranging from 0.6 to 125 MW of produced H_2 [5,12]. However, the operating voltage for splitting an H_2O molecule can be significantly reduced at high temperature. For this reason, SOEC can represent an attractive and effective solution, with an operative temperature in the intermediate range (500–650 °C) which appears as the optimum trade–off between durability and efficiency [13].

A typical rSOC is constituted by a solid electrolyte sandwiched between two porous electrodes. Among most commonly used materials for the electrolyte, fluorite-structured RE-doped ceria is considered the best candidate to operate SOC at the targeted operative temperatures [14-16]. Various oxides with perovskite [17-20], double perovskite [21-23] and Ruddlesden–Popper (RP) [24-26] structure showing suitable mixed ionic-electronic conductivity and/or electrocatalytic activity have been proposed for SOFC and SOEC electrodes layers.

Depending on the operating mode, each electrode can be the location where oxidation or reduction takes place. Global losses in such systems are related to the losses due to each component and it is widely proved that losses due to electrode processes can be lowered by an optimization of their microstructure, in terms of capability of gas exchange with gas phase as well as of ions migration. Among different strategies that have been pursued to improve the long-lasting time operation (durability), the infiltration of porous electrodes by discrete or continuous thin layers have been shown to be one of the most efficient. Main advantages of infiltration are: *i*) the electrode is fabricated by a two-steps deposition process, *i.e.* firstly a supporting porous backbone is deposited and sintered to get strong adhesion with the electrolyte, then the catalytic layer can be deposited and sintered at a lower temperature to keep optimal microstructure; *ii*) different coupling of backbone/catalyst can be used, since some fundamental parameters, such as TEC mismatch or chemical interactions can be minimized [27-29].

In literature it was already affirmed that BSCF material displays better performance under anodic polarization, suggesting that this material could be successfully used in a reversible SOFC–SOEC systems [30]. Moreover, the authors have already experienced the positive effect of LSM–infiltrated nano-sized layer on porous backbones, used in oxygen reduction conditions, finding that infiltration resulted in improved activity performance as well as durability [31].

In this study, a similar approach is carried out, to investigate the influence of LSM-infiltration on BSCF porous electrode, to test its catalytic activity in water reduction conditions, and evaluate BSCF-based material as possible electrode at the air side of rSOC.

2. Materials and Methods

The shape of the electrolyte support must respect appropriate geometric criteria. Namely, the distance between the reference electrode (RE) and working electrode (WE) should be at least three-times the electrolyte thickness, in order to avoid artefacts formation in impedance experimental spectra [17,32]. According to the relative shrinkage value obtained from previous sintering experience (22%), a weight of $Ce_{0.8}Sm_{0.2}O_{2-\delta}$ (SDC20) electrolyte powder equal to 2.4 g was uniaxially pressed at 37 MPa, to obtain electrolyte supports. The green pellets were sintered at 1500 °C for 5 h, obtaining sintered discs of 20 mm in diameter and 1.1 mm in thickness. Before the electrode deposition, the SDC discs were sanded down (P320 SiC paper) for obtaining a rough surface reliable for an easy adhesion of the BSCF electrode to the electrolyte layer.

A mixture of graphite (KS6, TIMCAL TIMREX®) and BSCF (Treibacher) powders, according to the 60/40 v/v% composition, was ball milled for 40 h at 40 rpm in distilled water, at R.T. and employing zirconia balls (Tosoh) as mixing bodies. This volume concentration was chosen in order to have a proper porosity resulting in an easy evacuation of the oxygen gas phase. After the mixing, a freeze-drying procedure was applied (24 h, at -52 °C and 22 Pa) and, finally, after sieving, the BSCF

powder was ready to be deposited. Alpha-terpineol (Sigma-Aldrich, >96%) was added to the powder (BSCF-graphite) in a mortar to obtain a mixture suitable for deposition. By applying an appropriate tape mask, a WE and a counter electrode (CE) were slurry coated on the sides of the SDC pellets. A RE, used for the three–electrode impedance measurements, was applied around the WE. The geometry is described in detail elsewhere [33]. The electrodes were co-sintered at 1100 °C for 1 h. After the sintering process geometric area for both the WE and the CE was 0.28 cm^2.

For the infiltration of porous BSCF electrode backbone, an aqueous solution of hydrated nitrates, namely $La(NO_3)\cdot 2H_2O$, $Sr(NO_3)_2$ and $Mn(NO_3)_3\cdot xH_2O$, with x = 4 or 6, was prepared. In order to estimate the actual cation concentration in precursors, a gravimetric titration of above-mentioned nitrates was carried out. About 5 g of each precursor were weighted out in a clean and dry Pt crucible and heated up to 900 °C for 2h, in order to allow for the formation of oxides, *i.e.* La_2O_3, SrO and Mn_3O_4.

The impregnating solution was prepared by adding stoichiometric amounts of hydrated nitrates, reported in Table 1, to 50 ml of water, in order to obtain a concentration of 0.6 mol l^{-1}. Glycine and polyvinylpyrrolidone (PVP) were added, respectively, as a chelating agent and as a surfactant (see Table 1) and the solution was heated at 200 °C under stirring for 10 min to completely dissolve the components. Impregnation was carried out by using different amounts of the nitrate solution, in the range 1.5 - 6 µl, either as-prepared or diluted. The samples tested in this work were impregnated with 1.5 µl of a solution with a concentration of 0.06 mol l^{-1}. In order to eliminate air in the pores, infiltrated samples were placed under a vacuum at 94 Pa for 2 min. The infiltrated cells (both in the WE and the CE), were finally heated at 800 °C for 3 h, with a 1 h dwelling step at 300 °C.

LSM-BSCF/SDC/LSM-BSCF half-cells (with a RE) were tested inside a ProboStat setup system (NorECs). Two Pt nets were placed on the surface of each electrode as current collectors. Electrochemical impedance spectroscopy (EIS) measurements were carried out through a Solartron Analytical potentiostat (SI 1286) coupled with a frequency response analyzer (SI 1255), and the ZPLOT software (Scribner Associates). Impedance tests were run between 475 and 650 °C, in a frequency range 10^4–10^{-2} Hz. An amplitude varying between 5 and 20 mV was applied, according to the system response. Measurements were performed at open circuit voltage (OCV) conditions as well as under anodic overpotential load, up to +0.2 V. An N_2/O_2 = 80/20 v/v% mixture was fed at both sides of the cell, corresponding to a flow of 40 Nml min^{-1} and 10 Nml min^{-1} of N_2 and O_2, respectively. To test the system durability, a 48-h long-lasting test was run under an anodic potential of +0.150 V, extracting an OCV impedance test every 6 hours.

To investigate the morphology and the adhesion between the layers an observation was performed by scanning electron microscopy (SEM, Phenom Pro-X) equipped with EDXS (Bruker) on the as-sintered and tested samples, in order to check the distribution of LSM on the top and cross the section of the BSCF electrode.

Table 1. Composition of $La_{0.8}Sr_{0.2}MnO_{3-\delta}$-infiltrated layer.

$La(NO_3)_2\cdot 2H_2O$	$Sr(NO_3)_2$	$Mn(NO_3)_3\cdot xH_2O$	Glycine	PVP
10.477 g	0.622 g	7.289 g	2.468 g [1]	1.158 g [2]

[1] 1/4 of the total molar amount of starting nitrates; [2] 0.05 wt% of LSM amount.

3. Results and discussion

3.1. Microstructural

In Fig. 1 the surface SEM images of the pristine BSCF and the 1.5 µl, 0.06 mol l^{-1} LSM-infiltrated electrode are reported, before and after the electrochemical characterisation. In the following, the LSM-infiltrated BSCF will be named just LSM-BSCF electrode.

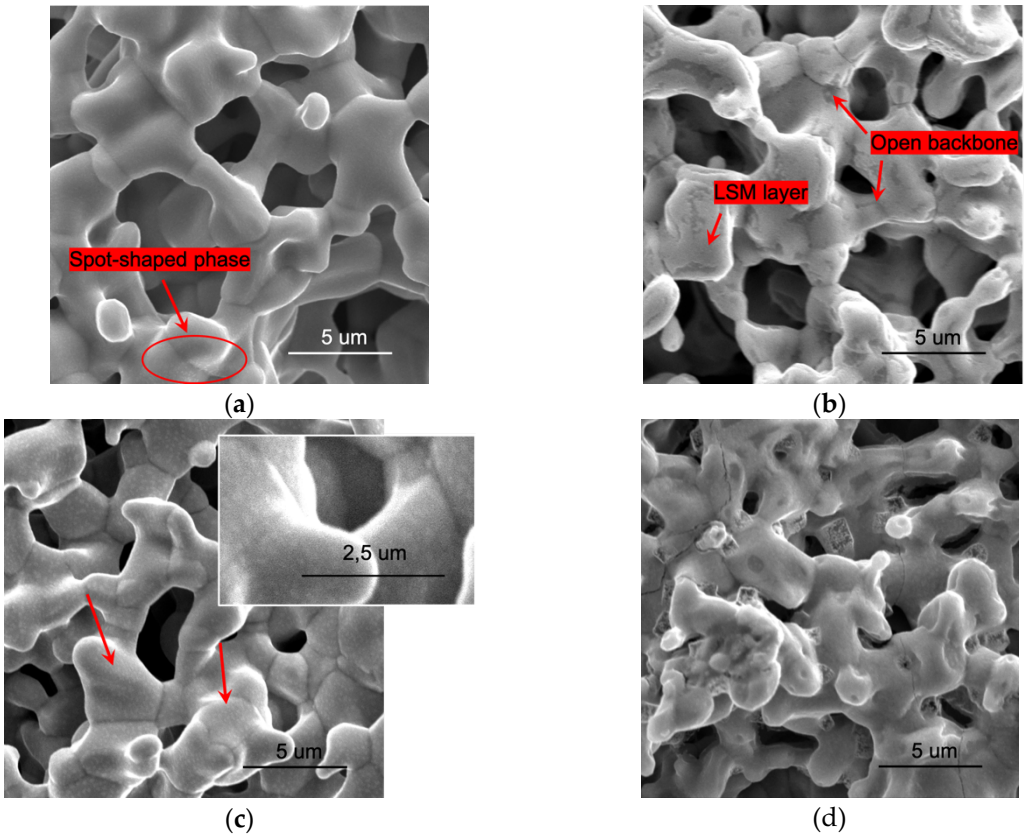

Figure 1. Surface SEM images of pristine BSCF (a, c) and of LSM-BSCF (b, d) electrodes before (top images) and after (bottom images) the electrochemical testing. Inset in (c) shows an improved view of spot-shaped phase. BSCF backbones were sintered at 1100 °C for 1 h.

After the sintering process at 1100 °C the electrodes showed a homogeneous structure, with open porosity and an appreciable coarsening of the grains, resulting in the formation of a good interconnected ceramic network (see Fig. 1).

By comparison of the images obtained before (Fig 1. (a) and (c)) and after the electrochemical testing (Fig. 1 (c) and (d), no apparent modification of the porous structure appeared. By contrast, transformations in the surface structure were evident for both electrodes after the electrochemical investigation. On the surface of the blank BSCF electrode a spot-shaped minor phase appeared (Fig. 1 (c)); likewise previous findings [31], it was supposed that this phase could result from the aggregation, during testing time between 475 and 650 °C, of the distributed phase before present on the BSCF starting electrode surface (see Fig. 1 (a) and (c), red arrows). Concerning the infiltrated electrode, the LSM infiltrated layer was obtained as a continuous layer (Fig. 1 (b)) and, after the testing, it showed in turn a structural modification (see Fig. (d)). *Sono deficiente ma non ho fatto l'analisi in quelle zone della Figura (d) che appaiono diverse dopo il testing. E non so come giustificarle… Nel caso non so se sono ancora in tempo per un'analisi: domani e dopodomani ho esami tutto il giorno.*

Figure 2 shows a SEM surface image of the LSM-infiltrated layer and the corresponding atomic concentration obtained through a map elemental analysis. Further EDXS observations performed through the cross-section of the infiltrated electrode, confirmed the penetration of the LSM layer up to the electrode/electrolyte interface.

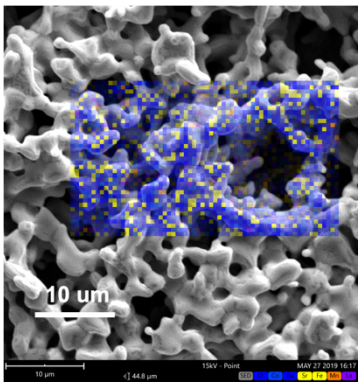

(**a**)

Element Number	Element Symbol	Element Name	Atomic Conc.	Weight Conc.
8	O	Oxygen	45.59	12.91
27	Co	Cobalt	19.23	20.06
56	Ba	Barium	16.89	41.05
38	Sr	Strontium	10.19	15.81
26	Fe	Iron	4.74	4.68
25	Mn	Manganese	1.88	1.83
57	La	Lanthanum	1.48	3.65

(**b**)

Figure 2. SEM-EDXS of LSM-BSCF infiltrated electrodes (before testing). Surface SEM image (a) with corresponding atomic concentration obtained through a map elemental analysis (b).

3.2. Electrochemical

Fig. 3 reports t an optical image (a) of the partial side of SDC electrolyte with the slurry coated WE and RE, awhile the geometry features of the three-electrode configuration (b) are reported in Figure 3 (b). The measurements were performed using a RE in order to have accurate control of the WE potential, especially when an overpotential was applied.

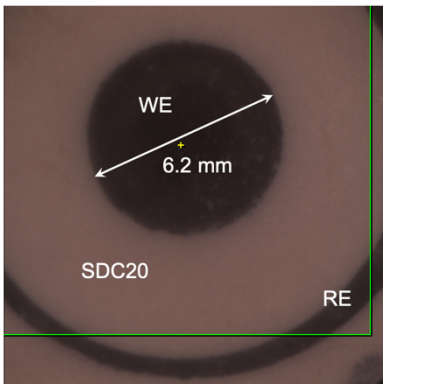

(**a**)

(**b**)

Figure 3. Image of the WE and RE on the SDC20 electrolyte (a); Probostat rig containing the sample to be tested (b).

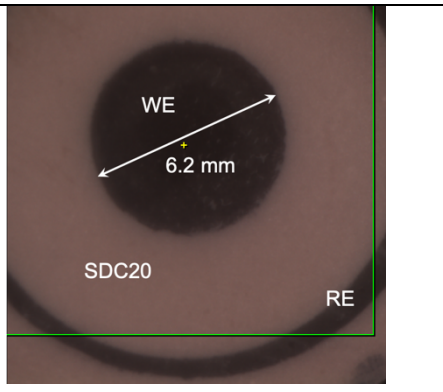

(**a**)

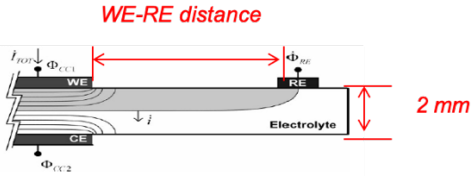

(**b**)

Figure 3. Image of the WE and RE on the SDC20 electrolyte (a); drawing of the three-electrode cell configuration (b).

First impedance measurements were carried out at OCV, then tests were run by applying an anodic overpotential, up to +0.2 V.

In Fig. 4 impedance spectra of blank BSCF (Fig. 4 (a)) and LSM-BSCF (Fig. 4 (b)) are shown. It is evident that the values of polarisation resistance (R_P), extracted as the difference between the low and high frequency intercepts with the real axys, are larger for the infiltrated electrodes than for pristine BSCF. At OCV and 650°C, the value of the area specific resistance (ASR) was 0.121 Ω cm² for the blank electrode and 0.148 Ω cm² for the infiltrated one. These results agree with other works, dealing with both blank and LSM-infiltrated electrodes [34-36]. Anyway, the polarisation resistance values obtained for the blank BSCF and LSM-BSCF infiltrated electrode are in contrast with previuos findings obtained by the authors on aLSM-infiltrated BSCF electrode. In that case [31], the LSM infiltration had a positive effect in terms of R_P at OCV. The reason of this discrepancy is likely due to the different morphology of LSM infiltrated layer. In the previous work we dealt indeed with a nano-sized discrete layer, resulting in increased electrode-gas surface exchance area and consequent improved electrode activity; in this study a continuous LSM layer was obtained, whose exchange properties with the gas phase are very different from those of the nano-distributed one.

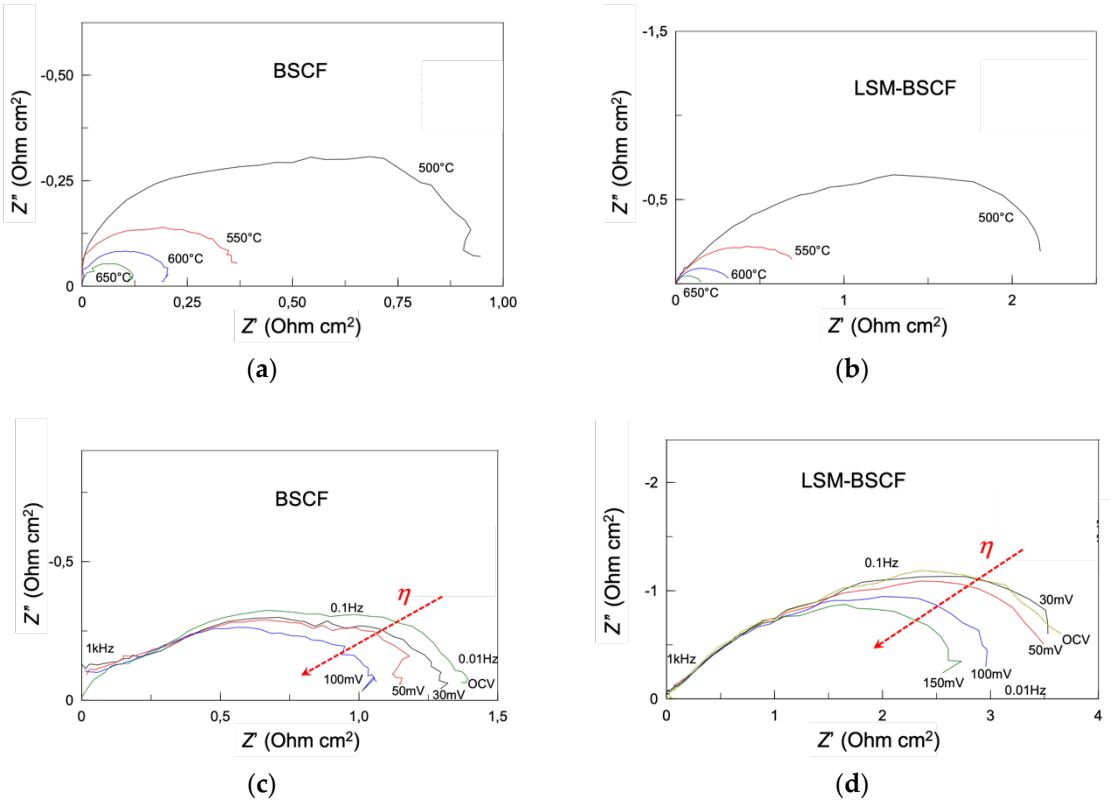

Figure 4. Impedance spectra at OCV between 500 and 650 °C of the blank BSCF (a) and infiltrated LSM-BSCF (b) electrode. Impedance spectra under anodic overpotential (η up to +0.150 V) for pristine BSCF (c) and LSM-BSCF infiltrated (d) electrode. Temperature conditions for (c) and (d): 475 °C. In every case SDC20 constitutes the electrolyte support. Measurements were performed in three-electrode configuration, using the ring-shaped RE.

Considering the effect of anodic overpotential (Fig. 4 (c) and (d)), it has a positive effect in terms of R_P values, both in case of blank and infiltrated samples. It was already found in previous study that cathodic overpotential had on the contrary a negative influence on the electrocatalytic performance of BSCF-based electrodes [17]. The positive effect of anodic overpotential was further confirmed through a sweep voltammetry measurement. Although not reported in the paper, the current density measured under anodic overpotential was slighly higher than that under cathodic overpotential, indicating a higher activity in anodic conditions (namely, when the electrode is involved as anode in electrolysis mode of operation).

Anyway, the presence of LSM did not improve the trend of impedance when η was increased. At the temperature of 475 °C, R_P at OCV was 1.37 Ω cm² for LSM-BSCF, while decreased until 1.06 Ω cm² for the blank electrode. For the latter, an ASR decrease of 22 % was observed under increasing anodic overpotential; the LSM-BSCF displayed an 18.6 % decrease between OCV and +0.100 V, becoming 28.5 % between OCV and +0.150 V. Unfortunately, beyond +0.1 and +0.15 V overpotential applied to the blank and infiltrated, respectively, electrodes were destroyed, appearing the infiltrated one more resistant.

In Fig. 5 the inverse of polarisation resistance ($1/R_P$) is reported as a function of temperature. An Arrhenius-like behaviour allowed for obtaining the values of apparent activation energy (E_a) for both the systems: 81 and 106 kJ mol^{-1} for blank BSCF and LSM-BSCF, respectively. These activation energy values concern the activity during the dynamic equilibrium state at OCV. Anyway, it has been proven in the literature that LSM activity drops under anodic conditions [37] and, actually, the impedance spectra extracted under anodic overpotential conditions confirm that the presence of the LSM hinders the activity of the electrode (see Fig. 4 (c) and (d)). Despite this detrimental effct due to LSM, the increase in the catalytic activity of the BSCF was confirmed when a net anodic current flows through the cell. As observable in Fig. 4 (d), the LSM hindering effect was not able to counterbalance the enhanced activity of BSCF. Moreover, LSM infiltrated layer resulted in a positive effect on the long-lasting performance of the SDC/LSM-BSCF system. In previous work, it was found out that LSM contributed to maintain the polarisation stability of BSCF electrode, likely because of a positive influence on the electrochemical potential gradient at the interface LSM/BSCF, being this stabilising effect indeed also observed for LSCF-based and other electrodes [14,17].

An anodic load of 0.150 V was run for 48 h at 600 °C and an impedance test was performed every 6 h. The result is shown in Fig. 5. It is observed that the activity behaviour, in terms of polarisation resistance, is stable for the duration of the test. During the voltage load, a current of 14 mA cm² was observed at 600 °C. This value should be certainly improved, but optimisation of the electrode morphology and performance under different gas partial pressures will be the subject of further investigations.

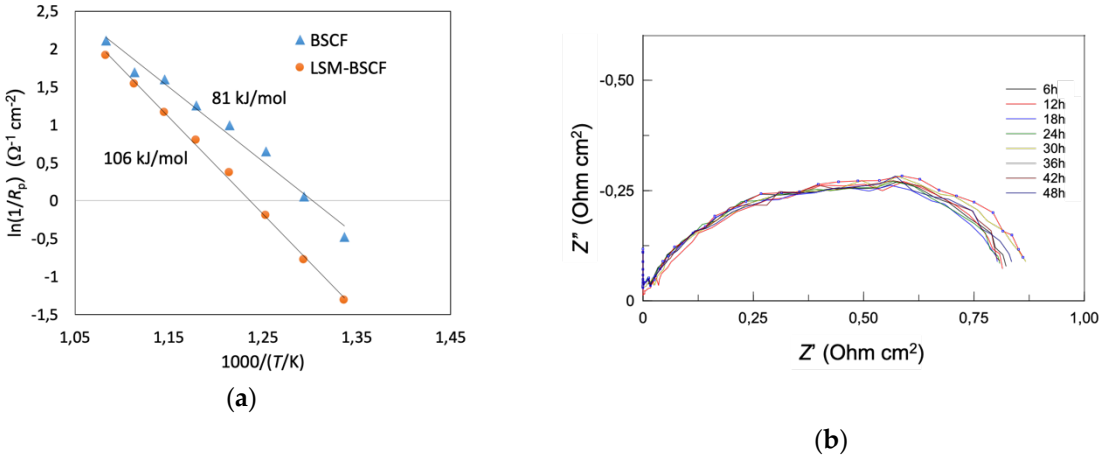

Figure 5. (a) Trend of the inverse of polarisation resistance (Rp) vs temperature, for blank BSCF and LSM-infiltrated BSCF. The values shown are the apparent activation energy from the linear

regression; (b) impedance spectra obtained for the LSM-BSCF electrode every 6 h, at OCV, during the anodic current load of +0.150 V for 48 h at 600 °C.

4. Conclusions

In this study blank BSCF and LSM-infiltrated BSCF electrodes are analysed, in view to be used as possible anode electrodes in solid state electrolysis (SOEC) devices. Electrochemical impedance spectroscopy investigation, coupled with ageing test at +0.15 V current load, was performed on a three-electrode system with SDC20 electrolyte.

It was found that polarization resistance decreases in both systems when an increasing anodic current load is applied. The blank BSCF electrode shows lower resistance (R_P) than the infiltrated one, then it appears that LSM does not give the chance to improve performance. This is possibly due to detrimental effect of the continuous LSM layer, covering most of the BSCF backbone. An LSM nano-sized discrete layer could result in increasing the surface exchange area, without subtracting appreciable BSCF surface and consequently making faster the gas-electrode activity. This was actually found out previously by the authors.

On the other hand, the LSM layer had a positive effect on the impedance stability, since no sign of degradation appeared in the first 48 h under a voltage load of +0.150 V. Performance degradation in the first 100 h of operation is one of the major problems to be faced in SOFC/SOEC devices and LSM infiltration demonstrated to be a promising approach in overcoming this issue. Further attempts have to be actually carried out in order to find the optimized parameters for a nano-sized discrete layer of LSM to be deposited. Most important, it was confirmed that BSCF-based electrodes are a very promising candidates to be used as oxygen electrodes in rSOC.

Author Contributions: conceptualization, M.P.C., A.B., G.C. and R.B.; methodology, M.P.C., A.B. M.V. and S.P.; software, M.P.C., M.V., D.Cle.; formal analysis, M.P.C., X.M.I., D.Cle. and D.Cad.; investigation, X.M.I.; resources, M.P.C., G. Cer.; S.P and R.B.; data curation, M.P.C., X.M.I.; writing—original draft preparation, M.P.C, X.M.I., M.V and D. Cad..; writing—review and editing, M.P.C.; visualization, M.P.C and X.M.I.; supervision, M.P.C.; funding acquisition, A.B., G.Cab, and G. Cer.

Funding: This research was funded in part by the Regional Council of Bourgogne Franche-Comté and the French National Center for Scientific Research (CNRS) Graduate School EIPHI (Contract ANR-17-EURE-0002) and through a visiting researcher position granted to M.P.C.

Acknowledgments: M. Paola Carpanese acknowledges the University of Genova for funding resources coming from FRA – Fondi di Ricerca di Ateneo 2018.

Conflicts of Interest: The authors declare no conflict of interest.

References

[1] European Commission, A European Green Deal, https://ec.europa.eu/info/strategy/priorities-2019-2024/european-green-deal_en.

[2] Gupta, R.; Soini, M.C.; Patel, M.P.; Parra, D. Levelized cost of solar photovoltaics and wind supported by storage technologies to supply firm electricity. J. *Energy Storage* **2020**, 27, 101027.

[3] Zsiborács, H.; Hegedüsné Baranyai, N.; Vincze, A.; Zentkó, L.; Birkner, Z.; Kinga, M.; Pintér, G. Intermittent Renewable Energy Sources: The Role of Energy Storage in the European Power System of 2040. *Electronics* **2019**, 8, 729.

[4] Mogensen, M.B.; Chen, M.; Frandsen, H.L.; Graves, C.; Hansen, J.B.; Hansen, K.V.; Hauch, A.; Jacobsen, T.; Jensen, S.H.; Skafte, T.L.; Sun, X. Reversible solid-oxide cells for clean and sustainable energy. *Clean Energy* **2019**, 3 (3), 175-201.

[5] Venkataraman, V.; Pérez-Fortes, M.; Wang, L.; Hajimolana, Y.S.; Boigues-Muñoz, C.; Agostini, A.; McPhail, S.J.; Maréchal, F.; Van Herle, J.; Aravind, P.V. Reversible solid oxide systems for energy and chemical applications – Review & perspectives. *J. Energy Storage* **2019**, 24, 100782.

279 [6] Perna, A.; Minutillo, M.; Jannelli, E. Designing and analyzing an electric energy storage system based on
280 reversible solid oxide cells. *Energ Convers Manage* **2018**, 159, 381-395.
281 [7] Giarola, S.; Forte, O.; Lanzini, A.; Gandiglio, M.; Santarelli, M.; Hawkes, A. Techno-economic assessment
282 of biogas-fed solid oxide fuel cell combined T heat and power system at industrial scale. *Appl Energy* **2018**,
283 211, 689-704.
284 [8] Carpanese, M.P.; Panizza, M.; Viviani, M.; Mercadelli, E.; Sanson, A.; Barbucci, A. Study of reversible
285 SOFC/SOEC based on a mixed anionic- protonic conductor. *J Appl Electrochem* **2015,** 45, 657–665.
286 [9] Thorel, A.S.; Chesnaud, A.; Viviani, M.; Barbucci, A.; Presto, S.; Piccardo, P.; Ilhan, Z.; Vladikova, D.
287 Stynov, Z. IDEAL-cell, a high temperature innovative dual mEmbrAne fuel cell. *ECS Trans* **2009**, 25:2 (part
288 1), 753-762.
289 [10] Gondolini, A.; Mercadelli, E.; Sangiorgi, A.; Sanson, A. Integration of Ni-GDC layer on a NiCrAl metal
290 foam for SOFC application. *J Eur Ceram Soc* **2017,** 37, 1023–1030.
291 [11] Zheng, Y.; Wang, J.; Yu, B.; Zhang, W.; Chen, J.; Qiao, J.; Zhang, J. A review of high temperature co-
292 electrolysis of H_2O and Co2 to produce sustainable fuels using solid oxide electrolysis cells (SOECs): advanced
293 materials and technology. *Chem Soc Rev* **2017**, 46, 1427-1463.
294 [12] Brauns, Z.; Turek, T. Alkaline Water Electrolysis Powered by Renewable Energy: A Review. *Processes*
295 **2020**, 8, 248.
296 [13] Laguna-Bercero, M.A. Recent advances in high temperature electrolysis using solid oxide fuel cells: A
297 review. *J Power Sources* **2012**, 203, 4-16.
298 [14] Presto, S.; Artini, C.; Pani, M.; Carnasciali, M.M; Massardo, S.; Viviani, M. Ionic conductivity and local
299 structural features in $Ce_{1-x}Sm_xO_{2-x/2}$. *Phys Chem Chem Phys* **2018**, 20, 28338–28345.
300 [15] Chen, G.; Sun, W.; Luo, Y.; He, Y.; Zhang, X.; Zhu, B.; Li, W.; Liu, X.; Ding, Y.; Li, Y.; Geng, S.;Yu, K.
301 Advanced Fuel Cell Based on New Nanocrystalline Structure $Gd_{0.1}Ce_{0.9}O_2$ Electrolyte. *ACS Appl Mater*
302 *Interfaces* **2019**, 11, 10642–10650.
303 [16] Jaiswal, N.; Tanwar, K.; Suman, R.; Kumar, D.; Upadhyay, S.; Parkash, O.; Uppadhya, S.; Parkash, O. A
304 brief review on ceria based solid electrolytes for solid oxide fuel cells. *J Alloys Compd* **2019**, 781, 984–1005.
305 [17] Singh, S.; Singh, P.; Viviani, M.; Presto, S. Dy doped $SrTiO_3$: A promising anodic material in solid oxide
306 fuel cells. *Int J Hydrogen Energy* **2018**, 43, 19242–19249.
307 [18] Clematis, D.; Barbucci, A.; Presto, S.; Viviani, M.; Carpanese, M.P. Electrocatalytic activity of perovskite-
308 based cathodes for solid oxide fuel cells. *Int J Hydrogen Energy* **2019**, 44, 6212–6222.
309 [19] Luo, H.; Wang, H.; Chen, X.; Huang, D.; Zhou, M.; Ding, D. Cation deficiency tuning of $LaCoO_3$
310 perovskite as bifunctional oxygen electrocatalysts. *Chem Cat Chem* **2020**, cctc.201902392.
311 [20] Carpanese, M.P., Clematis, D., Bertei, A., Giuliano, A., Sanson, A., Mercadelli, E., Nicolella, c, Barbucci,
312 A. Understanding the electrochemical behaviour of LSM-based SOFC cathodes. Part I — Experimental and
313 electrochemical. *Solid State Ion* **2017**, 301, 106-115.
314 [21] Niu, B.; Lu, C.; Yi, W.; Luo, S.; Li, X.; Zhong, X.; Zhao, X.; Xu, B. In-situ growth of nanoparticles-
315 decorated double perovskite electrode materials for symmetrical solid oxide cells. *Appl Catal B Environ* **2020**,
316 270, 118842.
317 [22] Presto, S.; Kumar, P.; Varma, S.; Viviani, M.; Singh, P. Electrical conductivity of NiMo–based double
318 perovskites under SOFC anodic conditions. *Int J Hydrogen Energy* **2018**, 43, 4528–4533.
319 [23] Rath, M.K.; Lee, K. Superior electrochemical performance of non-precious Co-Ni-Mo alloy catalyst-
320 impregnated $Sr_2FeMoO_{6-\delta}$ as an electrode material for symmetric solid oxide fuel cells. *Electrochim Acta* **2016**,
321 212, 678–685.

322 [24] Sharma, R.K.; Burriel, M.; Dessemond, L.; Bassat, J.-M.; Djurado, E. $La_{n+1}Ni_nO_{3n+1}$ (n = 2 and 3) phases
323 and composites for solid oxide fuel cell cathodes: Facile synthesis and electrochemical properties. *J Power*
324 *Sources* **2016**, 325, 337–345.
325 [25] Arias-Serrano, B.I.; Kravchenko, E.; Zakharchuk, K.; Grins, J.; Svensson, G.; Pankov, V.; Yaremchenko,
326 A. Oxygen-Deficient $Nd_{0.8}Sr_{1.2}Ni_{0.8}M_{0.2}O_{4-\delta}$ (M = Ni, Co, Fe) Nickelates as Oxygen Electrode Materials for
327 SOFC/SOEC. *ECS Trans* **2019**, 91, 2387–2397.
328 [26] Wang, J.; Zhou, J.; Yang, J.; Zong, Z.; Fu, L.; Lian, Z.; Zhang, X.; Wang, X.; Chen, C.; Ma, W.; Wu, K.
329 Nanoscale architecture of $(La_{0.6}Sr_{1.4})_{0.95}Mn_{0.9}B_{0.1}O_4$ (B=Co, Ni, Cu) Ruddlesden–Popper oxides as efficient and
330 durable catalysts for symmetrical solid oxide fuel cells. *Renew Energy* **2020**, 157, 840–850.
331 [27] Khoshkalam, M.; Tripković, Đ.; Tong, X.; Faghihi-Sani M.A.; Chen M.; Vang Hendriksen, P. Improving
332 oxygen incorporation rate on $(La_{0.6}Sr_{0.4})_{0.98}FeO_{3-\delta}$ via $Pr_2Ni_{1-x}CuxO_{4+\delta}$ surface decoration. *J Po*wer Sources
333 **2020**, 457, 228035.
334 [28] Ding, D.; Li, X.; Lai, S.Y.; Gerdes, K.; Liu, M. Enhancing SOFC cathode performance by surface
335 modification through infiltration. *Energy Environ Sci* **2014**, 7, 552-575.
336 [29] Jiang, S.P. A review of wet impregnation—An alternative method for the fabrication of high performance
337 and nano-structured electrodes of solid oxide fuel cells. *Mat Sci Eng A*, **2006,** 418, 199–210.
338 [30] Aguadero, A.; Pérez-Coll, D.; Alonso, J.A.; Skinner, S.J.; Kilner, J. A New family of Mo-Dioped $SrCoO_{3-\delta}$
339 Perovskites for Application in Reversible Solid State Electrochemical Cells. *Chem Mater*, **2012**, 24, 2655-
340 2663.
341 [31] Giuliano, A.; Carpanese, M.P.; Clematis, D.; Boaro, M.; Pappacena, A.; Deganello, F.; Liotta, L.F.;
342 Barbucci, A. Infiltration, Overpotential and Ageing Effects on Cathodes for Solid Oxide Fuel Cells:
343 $La_{0.6}Sr_{0.4}Co_{0.2}Fe_{0.8}O_{3-\delta}$ versus $Ba_{0.5}Sr_{0.5}Co_{0.8}Fe_{0.2}O_{3-\delta}$. *J Electrochem Soc* **2017**, 164 (10) F3114-F3122.
344 [32] Winkler, J.; Hendriksen, P.V.; Bonanos, N.; Mogensen, M. Geometric requirements of solid electrolyte
345 cells with a reference electrode. *J Electrochem Soc* **1998**, 145, 1184-1192.
346 [33] Carpanese, M.P., Giuliano, A., Panizza, M., Mercadelli, E., Sanson, A., Gondolini, A., Bertei, A.
347 Experimental Approach for the study of SOFC cathodes. *Bulg Chem Commun* **2016**, 48, 23-29.
348 [34] Meng, L.; Wang, F.; Wang, A.; Pu, J.; Chi, B.; Li, J. High performance $La_{0.8}Sr_{0.2}MnO_3$-coated
349 $Ba_{0.5}Sr_{0.5}Co_{0.8}Fe_{0.2}O_3$ cathode prepared by a novel solid-solution method for intermediate temperature solid
350 oxide fuel cells. *Chines J Catal*, **2014**, 35, 38-42.
351 [35] Deganello, F.; Liotta, L.F.; Marcì, G.; Fabbri, E.; Traversa, E. Strontium and iron-doped barium cobaltite
352 prepared by solution combustion synthesis: exploring a mixed-fuel approach for tailored intermediate
353 temperature solid oxide fuel cell cathode materials. *Mater Renew Sustain Energy* **2013,** 2:8.
354 [36] Yang, X.; Li, R.; Yang, Y.; wen, G.; Tian, D.; Lu, X.; Ding, Y.; Chen, Y.; Lin, B. Improving stability and
355 electrochemical performance of $Ba_{0.5}Sr0.5Co_{0.2}Fe_{0.8}O_{3-\delta}$ electrode for symmetrical solid oxide fuel cells by Mo
356 doping. J ALLOY COMPD *J Alloy Compd* **2020**, 831, 154711.
357 [37] Chen, X.J.; Khor, K.A.; Chan, S.H. Electrochemical behavior of $La(Sr)MnO_3$ electrode under cathodic and
358 anodic polarization. *Solid State Ion* **2004**, 167, 379-387.
359

360